Atomic Layer Deposition for Advanced Electrode Design in Photoelectrochemical and Triboelectric Systems

DOI: 10.1002/admi.201600835 Jingjie Su, Zhaodong Li, Yanhao Yu, Xudong Wang*

J. Su, X. Wang, Beijing Institute of Nanoenergy and Nanosystems, Chinese Academy of Sciences; National Center for Nanoscience and Technology (NCNST), Beijing, 100083, P. R. China

Z. Li, Y. Yu, Department of Materials Science and Engineering, University of Wisconsin-Madison, Madison, WI 53706, USA **<qry>Please provide full academic titles for all authors (Dr. or Prof.)</qry>**

E-mail: xudong.wang@wisc.edu

Abstract

As a powerful and versatile thin film deposition technique, atomic layer deposition (ALD) has been increasingly involved in the manufacturing of many energy harvesting and storage devices. Compared to the applications of ALD in lithium ion batteries and supercapacitors, ALD in photoelectrochemical (PEC) electrode and triboelectric nanogenerators (TENGs) development is relatively new. Most current progress in these two promising directions is not quite comprehensively covered. This article intends to summarize the most recent and representative research regarding the application of ALD in the fabrication of PEC electrodes and TENG active materials. We first discuss ALD of nanostructured electrochemically ly active materials and surface coating for PEC photoelectrodes, and the corresponding influence on solar energy conversion efficiency and electrode stability are discussed and

compared. A unique high-temperature ALD-based approach, called surface-reaction-limited pulsed chemical vapor deposition (SPCVD) is then introduced as a new approach to the synthesis of 3D branched NW architecture, which offers tremendous advantages in photoelectrode design. At last, a new exploration of ALD in the field of mechanical energy harvesting is presented as an effective strategy to modify the dielectric property of polymer thin films for TENG development.

Keywords: atomic layer deposition; photoelectrochemical electrodes; surface protection; triboelectric nanogenerators

1. Introduction

Atomic layer deposition (ALD) is a powerful thin film deposition technique with merits of good surface conformality, precise thickness control, and broad selection of substrate material and geometries.[1] These advantages particularly meet the structural evolution demands towards miniaturization and 3D integration of modern electronic and energy devices. Fundamentally, the desirable features of ALD originate from its unique sequential, self-limiting surface reaction mechanism, where multiple precursors are introduced separately.[2] This operation principle avoids reactions in the vapor phase and thus eliminates the formation of any agglomerations or pinholes, resulting in conformal thin films on the underlying substrate.[3] The film thickness can be precisely controlled down to the sub-nanometer level by adjusting the number of deposition cycles. Meanwhile, the film composition can be easily tuned by varying the pulsing ratio of different precursors. Nowadays, plasma has been more frequently used in combination with regular thermal ALD

processes. Although most oxides, nitrides and sulfides can be synthesized by regular thermal ALD,[2, 4] the plasma enhancement can be realized with ALD at lower temperatures by activating precursor molecules using plasma discharge.[5] It is particularly useful for depositing thin films with high purity and uniformity using low reactive precursors. All these unique advantages make ALD very attractive in synthesizing or modifying functional thin films.

Accompanying the rapid development of energy harvesting and storage systems, ALD is involved in every important energy-related technology, including lithium ion batteries (LIBs), supercapacitors, solar cells, photoelectrochemical (PEC) water splitting and triboelectric nanogenerators (TENGs). On one hand, ALD can be used to directly synthesize the electrodes and/or electrolytes on various charge collecting templates. On the other hand, ALD can be used to deposit protective layers to stabilize the high-performance electrode and/or electrolyte materials.[6] The broad and long-term study of ALD in LIBs, supercapacitors and solar cells has led to a number of comprehensive review articles in these directions.[7] Recently, the rapid evolvement of PEC water splitting as an alternative solar energy harvesting approach has motivated numerous efforts on studying and developing photoelectrode materials, interfaces and nanoscale architectures.[8] The unique growth behavior and its merits have placed ALD among the leading fabrication tools for designing and creating high performance PEC electrodes. Nonetheless, the most up-to-date development of ALD in PEC is not quite comprehensively covered in the literature.[9] Furthermore, nanogenerators, as an emerging technology for mechanical energy harvesting,[10] also use ALD as a novel electrode development approach; whereas a review of this new topic does not exist at the time of writing. Therefore, to deliver complementary coverage of the ALD technique in advanced nanomanufacturing of energy-related systems, this article summarizes the most recent progress of the application of ALD in the fabrication

of PEC photoelectrodes, from the aspects of active materials loading, surface modification, and the design of 3D hierarchical nanostructures. The ALD-enabled property control and performance gain in triboelectric nanogenerator (TENG) active film development are discussed in detail.

2. ALD of Photoelectrode Materials

Owing to the unique nature of precise thickness control and conformal growth on complex nanostructures, ALD has drawn much attention in depositing photocatalytic materials for PEC water splitting.[11] Materials that have been successfully deposited by ALD for PEC electrode include CdS, ZnS, CdSe, ZnSe, GaAs, ZnO, Ta_2O_5, $SrTiO_3$, and TiO_2.[12]

One common strategy to raise the PEC photocurrent density is to deposit photocatalytic thin films on highly ly surface-area 3D nanostructured template, taking the advantage of conformal coating capability by ALD. Introducing highly conductive 3D "nanoskeleton" for ALD photocatalytic material coating could further improve the performance of PEC electrodes. Transparent conducting oxide (TCO) nanostructures have been used as the template for ALD for the purpose of enabling high efficient charge transport and collection. Peng et al. developed a porous TiO_2 PEC electrode by coating antimony-doped tin oxide (ATO) NP films (nanoATO) with rutile TiO_2 viavia ALD (**Figure 1**a).[13] The interconnected ATO network provided fast redox carrier diffusion, efficient electron collection and transport as well as excellent light absorption, which gave rise to a high short circuit photocurrent density of 0.58 mA cm^{-2} under the 100 mW cm^{-2} illumination with AM 1.5G filter (Figure 1b). Similarly, Noh et al. used single crystalline indium tin oxide (ITO) NW arrays grown on a stainless steel mesh as the PEC electrode scaffold (Figure 1c).[14] Polycrystalline anatase TiO_2 with a thickness of 36 nm was deposited onto the ITO NWs by ALD at 250 °C (Figure 1d). Owing to the large surface area offered by the ITO/TiO_2 core/shell NW structures, the

photocurrent density was ≈4 times higher than that of the TiO_2-coated stainless steel mesh electrode (Figure 1e). Nevertheless, the photocurrent density could not show further increase when the length of ITO NWs increased from 10 μm to 20 μm and above. This might be a result of the poor quality of ITO NWs and the charge transport was mainly carried by the ALD TiO_2 film.

While the traditional TCOs were found to be challenged in producing a high quality nanoscale framework, single crystalline NWs with simpler compositions might see more opportunities as ALD templates for developing high-performance PEC electrodes. For example, Wang et al.et al. synthesized Cl-doped ZnO NWs with metallic conductivity, and fabricated PEC electrodes by coating the NW surface with ALD TiO_2 film.[8d] The TiO_2 layer was deposited at 300 °C and consisted of polycrystalline anatase with a thickness of 20 nm (**Figure 2**a). TEM clearly showed the high quality NW core was not affected by the mild ALD TiO_2 conditions. Thus, a high photocurrent density of 2.0 mA cm^{-2} was obtained at zero bias, which was more than twice as much as that of TiO_2-coated undoped ZnO NW photoanode (Figure 2b). Highly conductive Si NWs were selected as ALD templates for PEC electrode fabrication. Other than regular TiO_2 coating, Weng et al.et al. present a PEC electrode with n-type Si NW core and a 30 nm p-type α-Bi_2O_3 shell as shown in Figure 2c.[15] The Bi_2O_3 film was deposited by regular thermal ALD at a temperature of 190 °C using $Bi(thd)_3$ and H_2O as precursors. The polycrystalline Bi_2O_3 film showed a monoclinic α phase with a lattice spacing of 3.3 Å (inset of Figure 2c). The Mott-Schottky analysis revealed that the as-deposited Bi_2O_3 film had a typical *p*-type semiconductor behavior. The as-prepared core–shell NW photoelectrode had a relatively low reflectance in the visible light region, and the PEC stability at fixed bias of 1V (vs. RHE) was over 16 hours. These Si/Bi_2O_3 core–shell

NW arrays effectively combined the light absorption ability of the Si NWs and the wide energy gap and chemical stability of Bi_2O_3 for water splitting.

ALD of photocatalytic materials, such as TiO_2 and α-Fe_2O_3, was also applied to non-oxide metallic nano-scaffolds, such as $TiSi_2$ nano-net for PEC electrodes.[16] Compared to NW structures, the 3D network of single crystalline $TiSi_2$ provided enhanced light absorption and larger semiconductor-electrolyte interface for PEC reactions. From the anatase $TiO_2/TiSi_2$ nano-nets structures, a photocurrent density of 0.6 mA cm^{-2} was achieved at 0 V vs vs Ag/AgCl in 0.05 M alkaline solution under the illumination of a 150 W Xenon lamp. In order to broaden the light absorption spectrum, α-Fe_2O_3 was selected to replace TiO_2 to coat the $TiSi_2$ nano-net for PEC electrode development. Iron tert-butoxide ($Fe_2(O^tBu)_6$) and H_2O were used as ALD precursors for Fe_2O_3 deposition. The crystallinity of the hematite film was further improved by post annealing at 500 °C in oxygen atmosphere. As shown in Figure 2d, the Fe_2O_3 coating was very uniform, and high-quality interface between Fe_2O_3 and $TiSi_2$ could be clearly observed. These features facilitated rapid and low-loss charge transfer from Fe_2O_3 to $TiSi_2$. As a result, a remarkable incident photon-to-current conversion efficiency (IPCE) of 46% was obtained at 400 nm. A high photocurrents of 1.6 mA cm^{-2} at 1.23 V (vs (vs RHE) was achieved under AM 1.5 G illumination in 1 M NaOH solution.

Recently, integration of ALD with nanostructured template was further extended to modulating the PEC kinetics by developing a high-performance capillary PEC electrode that perform water splitting reactions outside of the electrolyte body.[17] In this work, Li et al.et al. fabricated a 3D photoelectrode structure by ALD of amorphous TiO_2 films on mesoporous cellulose nanofiber (CNF) template followed by high-temperature annealing, which burned off CNF template leaving an anatase TiO_2 nanotube network (**Figure 3**a). Such TiO_2 photoanode was demonstrated to perform PEC water oxidation outside of the electrolyte,

where the electrolyte was supplied through the nano/micro-channels in the CNF film driven by the capillary force (Figure 3b). Tested from the same sample, the capillary PEC exhibited a saturating photocurrent density of 0.87 mA cm^{-2}, which was 107 % higher than that of in-electrolyte set up (Figure 3c). The performance gain of the capillary PEC electrode was mostly attributed to the better interface charge transport kinetics. As shown in Figure 3d and e, the *J–V* characteristics of cellulose-templated TiO_2 photoanode under interrupted illumination exhibited an obvious initial current spike in each J_{ph} cycle for in-electrolyte measurement, but a less distinguishable one for capillary design. Such anodic current spikes are the evidence of accumulated photoexcited holes at the catalyst-electrolytes interface owing to the surface trapping states on the photoanode or slow oxygen evolution reaction kinetics at the interface.[18] Li et al.et al. further showed that the modification of the calcination atmosphere after the ALD process can be used to engineer the chemical compounds of TiO_2 nanofibers and enable visible light photoactivity.[17] By annealing the TiO_2-coated CNF structures in vacuum (600 °C, 24 hours, 55 mTorr) instead of in an O_2 atmosphere, the final structure appeared black while the fibrous morphology was well preserved (**Figure 4**a). The black color was a result of an appreciable amount of carbon residues, which induced significant visible light absorption. Under 100 mW cm^{-2} AM 1.5G illumination, the PEC performance of vacuum annealed photoanode in capillary setup was ≈ 400 % higher than the one annealed in O_2 (Figure 4b). These enhancements were even larger (≈800%) under visible light illumination (Figure 4c).

Although ALD metal oxide exhibits many merits as a promising PEC photoanode material, one major limitation is its relatively large band gap, which intrinsically constrains the light absorption only within a small portion of the solar spectrum. This jeopardizes the energy conversion efficiency when metal oxides are used as the light absorber in PEC

systems. Doping foreign elements into metal oxide lattices has been one common approach to narrow the optical band gap and align the band edges properly with targeting redox reaction levels.[19] Owing to the layer-by-layer growth mechanism, ALD-based doping can be simply achieved by periodically adding dopant cycles into the regular ALD growth cycles of the host material. The dopant concentration can be controlled by adjusting the ALD cycle ratio between the host and dopant materials.[20] For example, nitrogen-doped TiO_2 films were grown by ALD using $TiCl_4$, NH_3 and water as precursors.[20a] The dopant concentration was well controlled up to 3.8 % by adjusting the ratio of TiO_2 growth cycle to TiN growth cycle to 1:3. The N-doped TiO_2 films exhibited appreciable photoactivity under visible light. However, the photocurrent was found to suffer from increased surface recombination due to N doping. Lin et al. reported the synthesis of 3% Mg doped Fe_2O_3 thin films by introducing one cycle of bis(ethylcyclopentadienyl)magnesium precursor into every five cycles of an Fe precursor (iron tert-butoxide).[21] The Mg-doped Fe_2O_3 was proven to be p-type. By directly depositing 5 nm Mg-doped Fe_2O_3 on 20 nm pristine Fe_2O_3 film, which was intrinsic n-type due to oxygen vacancies, a p-n homojunction was formed. The built-in field yielded 200 mV turn-on voltage reduction toward the cathodic direction, which is beneficial to the PEC performance.

3. ALD of Surface Protection Layer

Narrow bandgap semiconductors (e.g., e.g., Si and III-V group of composites) are promising candidates for constructing efficient photoelectrodes for PEC H_2 production due to their effective light absorption and rapid charge separation.[22] The largest obstacle to practical solar-to-H_2 conversion is the poor stability caused by surface corrosion during the electrochemical reaction. One predominate strategy of alleviating this drawback is to protect the electrode surface with chemically inert oxide thin films.[23] Among various deposition

techniques, ALD can grow conformal and pinhole-free oxides with precisely controlled film thickness, which is critical for maximizing the protection performance. Thus, ALD is considered as one of the most suitable techniques for growing the electrode protective layers.

Chen et al. initially attempted to use ALD-grown oxide film to protect a silicon photoanode in 2011.[24] By depositing 2 nm-thick polycrystalline TiO_2 as the protective layer and 3 nm-thick Ir as the catalyst layer, the silicon photoanode achieved an open-circuit voltage (V_{oc}) of ≈550 mV, with 8 hours stability in 1M alkaline solution (**Figure 5**a–c). The thickness of the TiO_2 film was an important factor that determined the overall performance of the photoelectrode. A thickness of 2 nm was found to be sufficient to sustain hours of continuous operation in corrosive environments, while still being thin enough to allow facile charge transport via tunneling (Figure 5d). Increasing the polycrystalline TiO_2 thickness could lead to a quick reduction of PEC performance as a consequence of the significantly enlarged hole tunneling impedance. Figure 5e presents the current–voltage curve of $Ir/TiO_2/SiO_2/p^+$-Si anodes, clearly showing the reduced current density after increasing the TiO_2 thickness from 1.2 nm to 11.6 nm. Specifically, the over potential for the oxygen-evolution reaction (OER) increased linearly by ≈21 mV nm^{-1}, resulting in an additional ≈200 mV voltage loss for a 12 nm-thick TiO_2 layer, even at a current density of 1 mA cm^{-2}.[25] In this ALD polycrystalline TiO_2 protecting method, the strict requirement of the film thickness makes it very difficult to further extending the operation time.

To address this dilemma, Hu et al. found that the amorphous ALD TiO_2 has a much better hole conductivity presumably originated from the structural disorder and/or chemical impurities (e.g., carbon or nitrogen).[26] Hall measurements showed that the concentration of electrons in the as-grown amorphous ALD TiO_2 was 4×10^{16} cm^{-3}. As a result, the film thickness could be rapidly increased to as high as 143 nm without jeopardizing any charge

transport property (**Figure 6**a,b). The silicon electrode with a layer of 4–143 nm-thick TiO_2 and Ni catalyst islands could yield a V_{oc} of ≈510 mV, and a saturated photocurrent density of 35 mA cm^{-2} with a Faradaic efficiency close to 100 % for O_2 production in 1 M KOH electrolyte (Figure 6c). Silicon electrodes with varied TiO_2 thicknesses exhibited similar photocurrent density-voltage (*J-V*) behaviors, confirming the superior hole conductivity of the amorphous TiO_2. The thick TiO_2 film with minimum pinholes could perfectly isolate the silicon surface from the corrosive electrolyte and thus significantly promoted the stability to over 100 hours (Figure 6d), outperforming most other surface protecting strategies.[23a, 23b, 24] In Figure 6d, the slight decrease in photocurrent density occurring at around 55 hours was caused by the unstable light intensity.

The ALD-based amorphous TiO_2 protecting approach can be seamlessly transferred to the optimization of other unstable semiconductor photoelectrodes, such as GaAs,[26-27] GaP,[26] $GaInP_2$,[28] silicon microwires,[29] CdTe,[30] and $BiVO_4$.[31] For three-dimensional PEC photoelectrodes, such as silicon microwires, ALD was still able to produce a conformal coating due to its unique self-limited sequential reaction mechanism.[29] As shown in Figure 6e, ALD-grown TiO_2 was extremely uniform on the surface of an individual silicon microwire. The homogeneous distribution of amorphous TiO_2 enabled a continuous operation of this photoanode in 1M alkaline conditions for more than 2200 hours, which was an improvement of orders of magnitude compared to the unprotected one (Figure 6f).**<qry>Please clarify what is meant by "the unprotected one" here and please amend the sentence accordingly.</qry>** The large discrepancy between the silicon microwires and planar silicon (2200 hours versus 100 hours) was mainly caused by the distinct photocurrent densities (4 mA cm^{-2} versus 35 mA cm^{-2}). Smaller photocurrent density would reduce the corrosion rate of silicon microwires.

The protecting performance of ALD TiO_2 can be further enhanced by adding a thin aluminum doped zinc oxide (AZO) layer.[32] Paracchino et al.et al. largely improved the stability of cuprous oxide (Cu_2O) PEC photocathode by coating nanolayers of ALD grown AZO and amorphous TiO_2. Figure 7a,b present the cross-sectional schematic and top view SEM image of the protected electrode, which contains FTO and Au as the conductive substrate, electrodeposited Cu_2O as the photoactive material, AZO and TiO_2 as the protective layers and platinum as the hydrogen evolution catalyst. Without surface protection, bare Cu_2O quickly experienced reductive decomposition and produced Cu as indicated by the *J-V* plot in Figure 7c. The current density rapidly decreased to zero within 5 minutes after completely consuming the Cu_2O (inset of Figure 7c). On the other hand, the ALD-protected electrode exhibited typical *J-V* curve of hydroxyl reduction (Figure 3d) with optimized ALD film thickness (approximately 20 nm AZO and 11 nm TiO_2). At the potential of 0 V versus the reversible hydrogen electrode (RHE), this photocathode achieved a photocurrent density of –7.6 mA cm^{-2} and an estimated Faradic efficiency of close to 100% in 1 M Na_2SO_4 electrolyte buffered at pH = 4.9. Unlike the silicon protection case, pristine ALD TiO_2 was found to be not sufficient for stabilizing the Cu_2O electrode. After 20 minutes PEC reaction, the photocurrent density diminished to zero for merely TiO_2 protected Cu_2O. This phenomenon was believed to be a result of the incomplete coverage and photoreduction of the Cu_2O at pinholes in the TiO_2 layer. Adding ZnO between Cu_2O and TiO_2 could partially solve this issue by providing a more uniform hydroxylated surface for TiO_2 to grow on, leading to a complete coating of TiO_2 on Cu_2O surface. Consequently, 33% of the photocurrent density can be maintained after 20 minutes hydrogen-evolution reaction (HER). The stability enhancement can be further amplified by annealing the AZO protected sample at 200 °C in air for 45 minutes. Annealed electrode can conserve 78% of original photocurrent density after 20 minutes HER (inset of Figure 7d). The increased stability was

speculated to be caused by the removal of residual water from the ALD layers and the restructuring of layers at the interface. Since no evidence of Cu_2O degradation was observed, the 22% photocurrent decline was attributed to electron traps in the protective TiO_2 aggravated by its amorphous state.

This Cu_2O protecting method was further improved by a low temperature steam annealing process.[33] As shown in Figure 7e, the photocathode was built with layered structure of FTO/Au/Cu_2O/AZO/TiO_2/RuO_x. Figure 7f compares the *J-V* curves of electrodes with and without steam treatment, where an obvious increase of plateau photocurrent density was observed. After thoroughly characterizing the crystallinity, electrical band structure and surface geometry of ALD TiO_2, the enhancement was attributed to the smoothed TiO_2 surface after steam treatment, which facilitated the homogeneous catalyst deposition. Simultaneously, such a smoothing process could possibly patch any defects and cracks on TiO_2 surface, resulting in a large improvement of the operational stability (more than 50 hours, Figure 7g). The successful protection of the ultrasensitive Cu_2O photoelectrode highlights the effectiveness and versatility of the ALD TiO_2 protecting strategy. This discovery notably accelerated the evolution of PEC photoelectrodes and will be a great milestone in the solar fuel production development.

4. High Temperature ALD for 3D NW PEC Electrodes

3D NW network represents a promising architecture that features an extremely large surface area as well as tunable electronic properties. These merits make 3D NW architecture exceptionally advantageous for the PEC systems, whose performance is dependent on surface reactions and bulk charge transportation. Synthesizing such a unique hierarchical nano-architecture faces a critical challenge – the coupling between the crystal growth rate and the precursor concentration, which always leads to large size variations inside narrow spaces.

This challenge is intrinsic to almost all NW synthesis approaches, regardless of the phase of precursors. Recently, Shi et al. developed a surface-reaction-limited pulsed chemical vapor deposition (SPCVD) technique as a derivative of ALD.[34] By mimicking the self-limited growth mechanism of ALD, SPCVD uses separated precursor pulses and high deposition temperature. It effectively decoupled the crystal growth from precursor concentration while retaining anisotropic 1D growth. For the first time, this technique realized a 3D NW architecture with a depth of tens of micrometers with enhanced PEC performance.[8c]

The SPCVD technique was initially demonstrated by the growth of single-crystalline anatase TiO_2 NRs.[34] The SPCVD TiO_2 growth was performed in an ALD system at a chamber temperature of ≈600 °C. $TiCl_4$ and H_2O vapor precursors were pulsed into the chamber for 1.5 s each and separated by N_2 purging for 60 s. Anodic aluminum oxide (AAO) nanochannels were first used to show the unique NRs growth capability of SPCVD. The AAO nanochannels were ≈53 μm long but only ≈250 nm wide. 600 cycles of SPCVD achieved uniform and dense coverage of TiO_2 NRs along the entire channel length (Figure 8a). The majority of the as-synthesized TiO_2 NRs had lengths and widths of 170–210 nm and 25-30 nm, respectively (Figure 8b). The resulting 3D TiO_2 NR architectures offered a roughness factor of 3000, which is nearly ten times higher than that of typical NW arrays. Through this technique, TiO_2 NRs can be grown on a variety of surfaces inside confined spaces, such as NW forests.[8c] Figure 8c demonstrates a uniform coverage of TiO_2 NRs on the entire surface of dense Si NW array backbones. For Si NWs with lengths of more than 20 μm and inter-NW spacing below 200 nm, no obvious variations of the NR distribution and uniformity were observed. In addition to straight nanochannels, successful TiO_2 NR growth was also achieved inside inverse opal structures that were fabricated from ≈200 nm

nanosphere templates (Figure 8d). All these results demonstrated the excellent versatility of the SPCVD technique for synthesizing TiO_2 NR arrays inside different material matrixes.

In order to achieve rational control of 3D NR growth, scanning transmission electron microscopy (STEM) was applied to observe the crystal nucleation and growth of TiO_2 at different stages of the SPCVD process.[35] **Figure 9** shows a series of HR-STEM images revealing the evolution of TiO_2 NRs at 600 ºC. At the beginning of growth (1−5 cycles), there are no noticeable TiO_2 morphologies (Figure 9a, b); while electron energy loss spectroscopy (EELS) analysis revealed the existence of Ti elements from the Si NW edge. At 10 cycles, three typical morphologies emerged as shown in Figure 9c: cloudy and loosen amorphous flakes with diameters ranging from 1 to 2 nm; ultrathin amorphous film covering the surface of Si NW with a thickness of several angstroms (inset of Figure 9c); and sparsely distributed fuzzy amorphous particles with a diameter of ≈1 nm. Co-exist of these three intermedia phases was regarded as a manifestation of the Ostwald-Lussac Law. When growth proceeded to 20 cycles, amorphous particles and ultrathin films became the dominating morphologies (Figure 9d). After 35 cycles of growth, the NW surfaces were covered with larger NPs (5−10 nm), which were the agglomeration of small crystallites shelled by thin amorphous layers (Figure 9e). As the growth proceeded to 50 cycles, the integrated NP assemblage became larger and its elongated shape appeared like embryos of NRs (≈10 nm wide and ≈20 nm long, Figure 1f). Both the HR-STEM image and its fast Fourier transform (FFT) (right inset of Figure 9f) show that most small crystallites in the NP assemblage had the same orientation. A thin amorphous layer was also observed in the outmost region of the bulk embryos. At 75 cycles, high-density miniature NR-like single crystals of ≈20 nm wide and ≈40 nm long started to form (Figure 9g). Eventually, typical TiO_2 NRs were received after longer growth cycles (Figure 9h). The entire NR evolution process is schematically shown in Figure 9i.

By using the TiO_2-Si heterogeneous 3D NW architecture, Shi et al. further demonstrated an enhanced PEC efficiency for photocatalytic water splitting reactions.[8c] As shown in Figure 10a, when this heterogeneous structure was used as a PEC anode for water splitting, photocatalyzed H_2O oxidation reactions only occurred on the TiO_2 surfaces. The photogenerated electrons would quickly transport through the Si NW backbone and reach the counter electrode with minimal losses owing to the high conductivity of Si NWs and isolation from electrolyte. The very large surface area provided by the TiO_2 NR arrays together with the high-speed electron transport channels provided by the Si NWs are promising features that could lead to a significant improvement of the PEC efficiency. To demonstrate the advantages of the 3D NW architectures as PEC anodes, performance of three TiO_2/Si NW-based configurations were characterized and compared. They were wet-etched Si NWs with TiO_2 NRs, dry-etched Si NWs with TiO_2 NRs, and wet-etched Si NWs coated with a ≈37 nm TiO_2 film. All the Si NW templates were 10 μm long. Figure 10b shows the photocurrent density of these three samples as functions of the bias potential under the illumination of 100 mW cm^{-2} Hg (Xe) arc lamp. Both NRs-coated samples exhibited significantly higher photocurrent density owing to their larger surface areas. The photocurrent density was also found increased monotonically as the length of Si NW backbone increased from 1.5 μm to 20 μm, suggesting effective charge transport could be achieved in the 3D NW architecture through large electrode thicknesses. The highest efficiency yielded by the TiO_2 NR-Si NW heterostructure was found to be 2.1%, which was more than three times higher than that of TiO_2 film-Si NW core-shell structures. This result suggested that implementing 3D NW networks into electrode design could advantageously impact the performance of PEC and photovoltaic devices.

Yu et al. et al. further applied SPCVD of TiO_2 NRs on ZnO NW backbones. Under high deposition temperature, ZnO NWs interacted with $TiCl_4$ precursor vapor and were quickly

converted into polycrystalline TiO_2 tubes following the Kirkendall effect.[36] The evolution of TiO_2 nanotubes from ZnO NW scaffolds was integrated with TiO_2 NR branch growth and thus realized a pure TiO_2-phased 3D NW architecture (Figure 10c). Because of the significantly enlarged surface area and the trace amount of Zn left in the TiO_2 crystals, such 3D TiO_2 nanoforests demonstrated enhanced PEC performance particularly under AM (air mass) 1.5G illumination. The achieved short circuit current density of the 3D TiO_2 nanoforest was ≈0.75 $mAcm^{-2}$, which was 7 times higher than the referenced TiO_2 film-ZnO NW sample (≈0.11 mA cm^{-2}). Li et al.et al., reported the high-density 3D TiO_2 fiber-NR heterostructure synthesized through integrating the SPCVD process with mesoporou cellulose nanofibers.[37] The ALD ZnO film overcoating on nanostructured CNF was used as template for SPCVD growth of TiO_2 NR branches. The ZnO layer was sacrificed following the vapor-phase Kirkendall effect, and seeded the growth of TiO_2 NRs with well-preserved CNF framework (Figure 10d). The as-synthesized 3D TiO_2 fiber-NR heterostructure was applied as the photoanode for efficient PEC water splitting. They offered significantly enlarged electrolyte-electrode interface area, long optical paths and high quality crystal channels for rapid charge separation and conduction. As a result, the photocurrents of the 3D TiO_2 fiber-NR heterostructure were found to be ≈240% higher than those of the cellulose-templated TiO_2-ZnO bilayer tubular nanofibers and TiO_2 nanotube networks (**Figure 11**). Meanwhile, more conspicuous photoactivity was achieved in visible wavelength regions, which was caused by the residual carbon-induced extra visible light absorption.

As a derivative of ALD, SPCVD also shares the ability of convenient doping to tailor the band structure of synthesized materials. By introducing designed number of TiN cycles to TiO_2 NR growth cycles, Li et al.et al. successfully synthesized nitrogen-doped TiO_2 NR branch architectures (**Figure 12**a).[20b] The TiN growth cycle was applied by introducing NH_3

vapor as additional precursor pulses between typical H_2O and $TiCl_4$ cycles for growing TiO_2 NRs at 600 °C. It was found nitrogen doping could impact the TiO_2 NR morphology. In general, the length of NRs slightly decreased from 143 ± 9 nm (the undoped NRs) to 137 ± 7 nm when the NH_3 cycle ratio was increased to 1:20. Meanwhile, the average diameter of the NRs monotonically decreased from 25 ± 4 nm to 19 ± 3 nm. When the NH_3 cycle ratio was further increased from 1:20 to 1:1, a large decrease of NR length from 137 ± 7 nm to 114 ± 9 nm was observed. The NR diameter also rapidly increased from 19 ± 3 nm to 34 ± 5 nm, indicating a significant change of NR morphology from long and slim to short and plump upon the introduction of N dopants.

The statistical size measurement provided a preliminary understanding of the TiO_2 NR growth behavior by SPCVD under the influence of an NH_3 precursor. This observation is similar to the ALD of N doped TiO_2 films because TiN has a lower growth rate than TiO_2. In SPCVD, the unique anisotropic crystal growth behavior of TiO_2 is enabled by the formation and migration of metastable amorphous−crystalline mix-phased NPs via the principle of solid state oriented attachment. Therefore, it was believed that the deposition of TiN had significantly hindered the aggregation and migration of the metastable NPs and thus suppressed the NR length growth. The significantly increased NR width growth rate evidenced the immobilization of the metastable NPs, which stayed at the side surfaces and induced faster width growth. Nevertheless, it appeared that a lower NH_3 ratio (<1:20) can reduce the width growth rate as well. Therefore, the aspect ratios of all samples followed a parabola-like curve as shown in Figure 12b. The maximum aspect ratio was 7.4 from TiO_2 NRs which had a NH_3 precursor ratio of 1:20. In general, low doping concentration had minimal effect on the TiO_2 NR's growth rate and morphology, while high doping concentration could jeopardize the anisotropic crystal growth and form more particle-like nanocrystals.

Electronically, the valence band maximum of nitrogen doped TiO_2 NRs exhibited a notable lifting up to ≈2.4 eV in the most highly doped sample (Figure 12c). The as-synthesized nitrogen-doped TiO_2 NR branched heterostructures were used as PEC photoanodes, and their performance was characterized within controlled illumination wavelength ranges. Figure 12d revealed the nitrogen-doped TiO_2 NRs had appreciable PEC activity in the visible light range from 450 to 700 nm. The maximum efficiencies offered by nitrogen doping were 225% higher than those of the undoped TiO_2 NRs under AM 1.5 G illuminations. The enhancement of PEC efficiency was more than 900% when only visible light was illuminated.

5. Application of ALD in Mechanical Energy Harvesting Device Design

Sequential infiltration synthesis (SIS) is a molecular infiltration process on the basis of the ALD technique.[38] When certain polymers are implemented, the large permittivity of metal-organic ALD precursors allows the deep infiltration of inorganic compounds during the ALD process, leading to inorganic/organic hybrid materials. SIS has been successfully used to convert the block co-polymer nanopatterns into more durable inorganic patterns and to improve the polymeric lithography resistance towards the subsequent etching.[39] Inspired by these developments, SIS was found effective in tailoring the internal composition and electrical properties of polymer films, which may provide an ultimate solution to modifying triboelectric materials in bulk volume, and hence improving the performance of triboelectric nanogenerator (TENG) for advanced mechanical energy harvesting.

Based on SIS, Yu et al. reported an internal AlO_x doping of several triboelectric polymers, including PDMS, polyimide (Kapton) and poly(methyl methacrylate) (PMMA).[6a, 40] AlO_x molecules were found to be capable of penetrating into these polymers as deep as ≈3

μm, which effectively tuned the bulk electrical property of the films. TENG devices using the modified polymer films exhibited enhanced power output; and this enhancement remained effective after the surface of polymer film was polished off for more than 2 μm. AlO_x was selected as the dopants since trimenthy aluminum **<qry>Should this be "trimethyl aluminium"?</qry>(**TMA, ALD precursor of Al_2O_3) has desirable permittivity in a number of polymers such as polystyrene (PS), PP, polyethylene (PE), and poly(vinyl chloride) (PVC) and PMMA.[38c] The SIS doping process was carried out in a homemade ALD system by sequentially introducing TMA and H_2O vapor to the polymer film at 80 °C with controlled exposure time and cycles. **Figures 13**a and b show the cross-sectional SEM images and corresponding energy dispersive spectroscopy (EDS) elemental mappings of the pristine PDMS film and the same film after 5-cycle sequential TMA/H_2O infiltration (marked as AlO_x-doped PDMS), respectively. PDMS elements including silicon (Si), oxygen (O) and carbon (C) were all identified with a uniform distribution in the pristine film, and no aluminum (Al) signal was detected (Figure 13a-ii-v). For the SIS-treated PDMS, an Al signal was clearly detected and was concentrated within the top ≈3 μm region, revealing the effective infiltration depth (Figure 13b-ii). Similarly, both O and C elements exhibited a concentrated signal within the top ≈3 μm region matching well with Al distribution (Figure 13b-iv and v). The concentrated O element was originated from Al-O bonds formed after H_2O molecule infiltrated into polymers and reacted with TMA. The unreacted methyl groups on TMA could be the main source responsible for the concentrated C signal. This elemental distribution analysis evidences the successful deep infiltration of both precursors in the polymer film, and no surface coating of Al_2O_3 was identified.

XPS characterizations further confirmed the presence of an Al element in the PDMS after the SIS infiltration. As shown in Figure 13c, a small peak of Al 2p appeared at the low

binding energy region from the AlO_x-doped PDMS film. The high resolution scan of the Al 2p signal demonstrated a peak shift from 75.6 eV to 74.7 eV after the SIS treatment, which was caused by the formation of the defective aluminum oxides such as Al_2O and AlO (Figure 13d). The nonstoichiometric aluminum oxide may introduce extra charge carrier sites and thus improve the charge capacitance of the modified PDMS film. This hypothesis was verified by the dielectric constant measurement (Figure 13e). SIS doping increased the dielectric constant of PDMS films from ≈2.4 to ≈2.7 within the test frequency range, implying that modified PDMS was capable of storing more charges compared with the pristine one.

Similar to other polymer modification strategies (e.g., fluorine plasma treating and ion injection),[40] the SIS doping could also arbitrarily tune the electron affinity of triboelectric polymers and modulate the charge attraction/repulsion ability. For the AlO_x doping case, aluminum oxide will lower the electron affinity of PDMS since AlO_x is a triboelectric positive material with high tendency to lose electrons. As a consequence, electron would be injected from AlO_x-doped PDMS to PDMS upon their frication, leading to a positively charged surface in the doped PDMS and negatively charged surface in the pristine PDMS (**Figure 14**a). On the contrary, two PDMS films without modification could not induce such a charge redistribution due to the identical surface potential. Therefore, the AlO_x doping process should be able to significantly raise the TENG performance. Figures 14b–d show the V_{oc}, J_{sc}, and the total amount of charge transferred under short-circuit condition (ΔQ_{sc}) of TENGs with two configurations: PDMS-PDMS and PDMS-AlO_x-doped PDMS. For pair of PDMS-AlO_x-doped PDMS, the average peak values of the V_{oc}, J_{sc}, and ΔQ_{sc} reached 2.3 V, 2.2 μA cm^{-2} and 45 μC m^{-2}, respectively, which were comparable to TENGs built with

typical triboelectric couples, such as teflon-metal pair.[41] In comparison, only 0.3 V of V_{oc}, 0.3 μA cm^{-2} of J_{sc} and 5 μC m^{-2} of ΔQ_{sc} were obtained for the untreated PDMS pair.

One unique advantage of this SIS doping method is the simultaneous surface and bulk modification of the polymer's electrical property. The bulk doping capability allowed the performance gain of TENGs to survive even after polishing off 2 μm thick polymer materials. Figure 14e presents the V_{oc} variation as a function of the removed thicknesses. ≈95% of V_{oc} was remained after 2 μm-thick material was polished. Such a durable TENG performance was contributed by the deep penetration (≈3 μm) of AlO_x dopants. Further polishing the film dramatically reduced V_{oc} due to the expose of unmodified PDMS. A minimum value of ≈0.3 V was received after removing 5 μm polymer, which was comparable to the TENG output with the pristine PDMS pair.

The up limit of this SIS doping process was revealed by varying the infiltration cycles and measuring the related TENGs output. As shown in Figure 14f, the peak V_{oc} was improved from 0.3 V to 1.9 V by only 2 cycles of SIS, suggesting the high effectiveness of this polymer modification approach. The V_{oc} kept increasing with the increment of SIS cycles and eventually saturated at ≈2.4 V after 10 cycles of infiltration. Almost stable values were recorded when further increasing the cycle numbers. This V_{oc} variation is believed to be a consequence of the unique reaction process of AlO_x in the polymer material. During the first 10 cycles of infiltration, TMA diffused into PDMS and accumulated inside the polymer film, resulting in the rapid increase of V_{oc}. After 10 cycles, more deposition might cover the entire PDMS surface and prevent further inside infiltration. Thus the growth mode switched back to regular ALD deposition of continuous Al_2O_3 film on the surface. Because additional cycles of

infiltration contributed no internal doping, the electric property and TENG output would not exhibit any further change.

Compared to other chemical modification techniques,[40] the SIS doping process extends the modification region from the surface to bulk portion of triboelectric polymers. This improvement is important for developing high-performance TENGs with good resistance to the surface wearing issue. Moreover, the SIS doping is versatile in tailoring broad range of triboelectric polymers since a variety of metalorganic molecules possess high permittivity in most polymer chains.[1] With proper selection of doping precursor and precise control of infiltration condition, SIS doping could be a promising strategy to engineering electric and dielectric properties of many polymers, and improving the performance of functional polymer based devices, such as TENGs.

6. Perspective Remarks and Conclusions

ALD has demonstrated great potential as a versatile fabrication technique for manufacturing many energy harvesting and storage devices with enhanced performances. The unique capability of conformal coating on complex nanostructured surfaces offers an unprecedented advantage for ALD in active material deposition and surface functionalization. As a relatively new fabrication technology in electrode development, ALD was found very effective to create novel nanostructures, stabilize the material interface, and tune the surface/bulk chemistry and electronic properties. Although many promising results have been discovered recently, applications of ALD in photocatalysis and mechanical energy harvesting are still in their early stage. Practical, particularly industrial level applications of ALD in these areas are facing several critical challenges currently.

First, compared to other methods of thin film deposition, such as CVD, sputtering or Sol–gel, the growth rate of ALD is much slower. The intrinsic slowness of ALD due to its cycle-by-cycle growth fashion may impose tremendous restriction to the improvement of production rate and reduction of fabrication cost. In this regard, surface modification instead of direct growth might see more rapid application pace due to the extremely low requirement on the quantity of material dosing. Meanwhile, development of fast ALD with the roll-to-roll processing capability will be greatly desired to reduce to fabrication time consumption and improve throughput.[42]

Second, ALD coating on powders/nanoparticles is becoming more and more popular and important in electrode material development. However, due to the extremely large surface areas and great contacting points/areas**<qry>Do you mean "many contacting points" here?</qry>**, particle-ALD is much more difficult compared to coating other surfaces, which may require specially designed ALD system. Fluidized particle bed reactor and rotary ALD reactor have been developed to perform ALD on powders.[43] In the fluidized particle bed system, sample powders are fluidized by inert gas flow to perform the regular ALD processes. It is more suitable for processing small quantity of samples. The rotary ALD system fluidizes sample powders by the rotation of the sample container inside the reactor or the reactor as a whole. It is able deal with large amount of samples but requires extra-long time for precursor exposure. In such dynamic ALD systems, new understanding of the precursor deliver and reaction kinetics are still needed in order to achieve more efficient precursor usage and better coating uniformity.

Third, similar to other ALD applications, new ALD chemistries are greatly desired. Although many ALD precursors have been developed and successfully used, such as halides, nitrates, sulfides and organometallic compounds, most of these precursors are far from

satisfactory, particularly for industry-level manufacturing. Developing new ALD precursors now becomes an essential aspect in the ALD industry. In order to achieve sustainable ALD manufacturing, the new precursors are preferred which are selectively reactive, safe, non-toxic, and cost effective.

Moreover, new ALD system design may need to be implemented to satisfy the increasing demand of ALD film production. For example, the spatial atmospheric ALD (AALD) emerged years ago as a new ALD approach.[44] It is a continuous ALD process that operates at or near atmospheric pressure. Different from the conventional ALD processes, the precursors in AALD system are separated in space rather than in time, thus eliminating the lengthy purging steps and the need of vacuum. Therefore, the AALD system is more advantageous for industrial-level manufacturing. It is particularly useful for electrode surface function or protection, which might be integrated into the manufacturing system as one critical processing step.

At last, new functionality based on ALD is being developed, which brings new capability in electrode or system fabrication. For example, high-temperature ALD-based SPCVD was developed to synthesize 3D branched NW architectures, which offer large surface area and high charge transport simultaneously, and have become very promising candidates as PEC photoelectrodes. Most recently, a potential application of ALD was explored in the field of mechanical energy harvesting, by demonstrating the ability to modify the dielectric property of polymer thin films in the development of TENGs.

In general, driven by the unique capability and this very intriguing potentials of ALD in the fabrication of energy-related devices, one can certainly see further developments and

broader integration of ALD-based techniques in the manufacturing of energy harvesting and storage systems.

Acknowledgements: The authors thank the support of U.S. Department of Energy (DOE), Office of Science, Basic Energy Sciences (BES), under Award No. DE-SC0008711; and the "Thousands talents" program for pioneer researcher and his innovation team, China.

Figures and Captions:

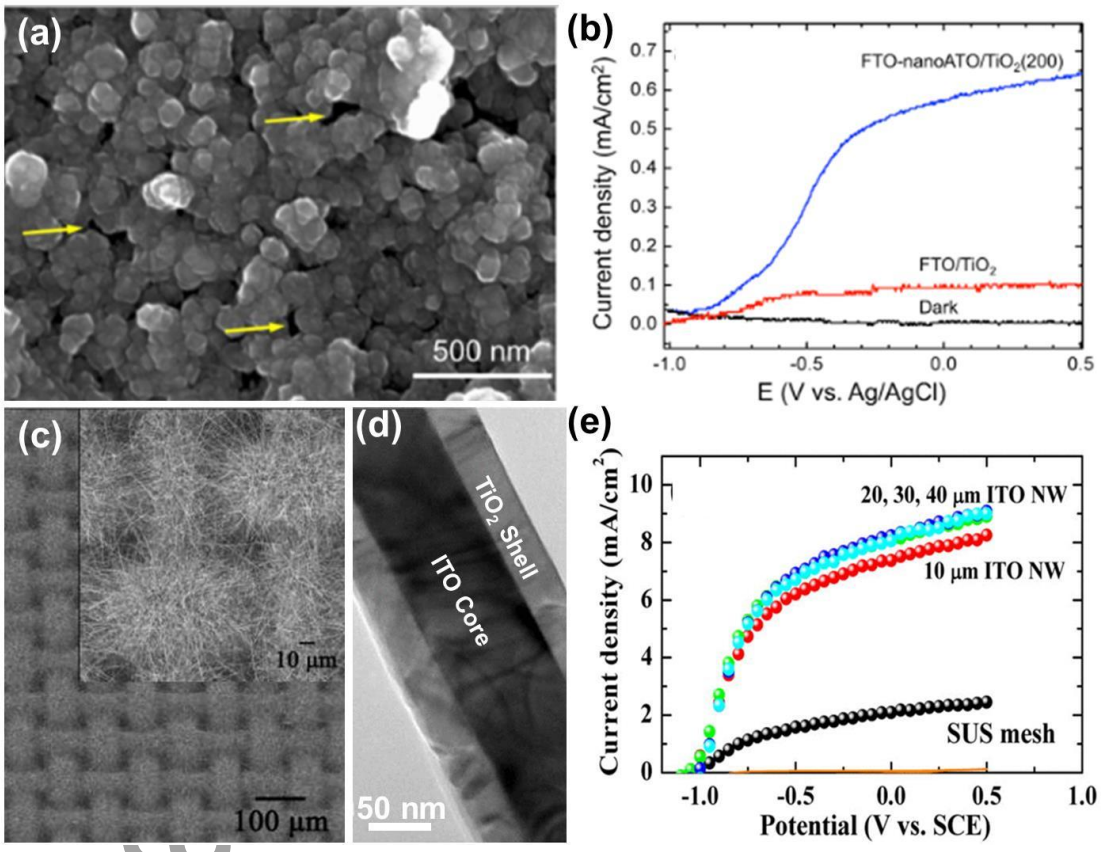

Figure 1. a) NanoATO film with 600 cycles of TiO_2 ALD coating. b) J–V characteristics of planar FTO/TiO_2 PEC electrode (red line) and FTO-nanoATO/TiO_2 electrodes (blue line), as well as the dark current curve (black line). Reproduced with permission.[13] Copyright 2013, American Chemical Society. c) ITO NW arrays grown on a stainless steel mesh. d) TEM image of an ITO core-TiO_2 shell NW. e) J–V characteristics of the TiO_2/ITO core-shell NW photoanodes under different NW lengths. The orange curve is the dark currents of all the specimens. Reproduced with permission.[14] Copyright 2012, AIP Publishing LLC.

All images were reproduced with permission from the
American Chemical Society [Copyright 2005 (a) and 2008 (c)] and Elsevier
[Copyright 2008 (b)].

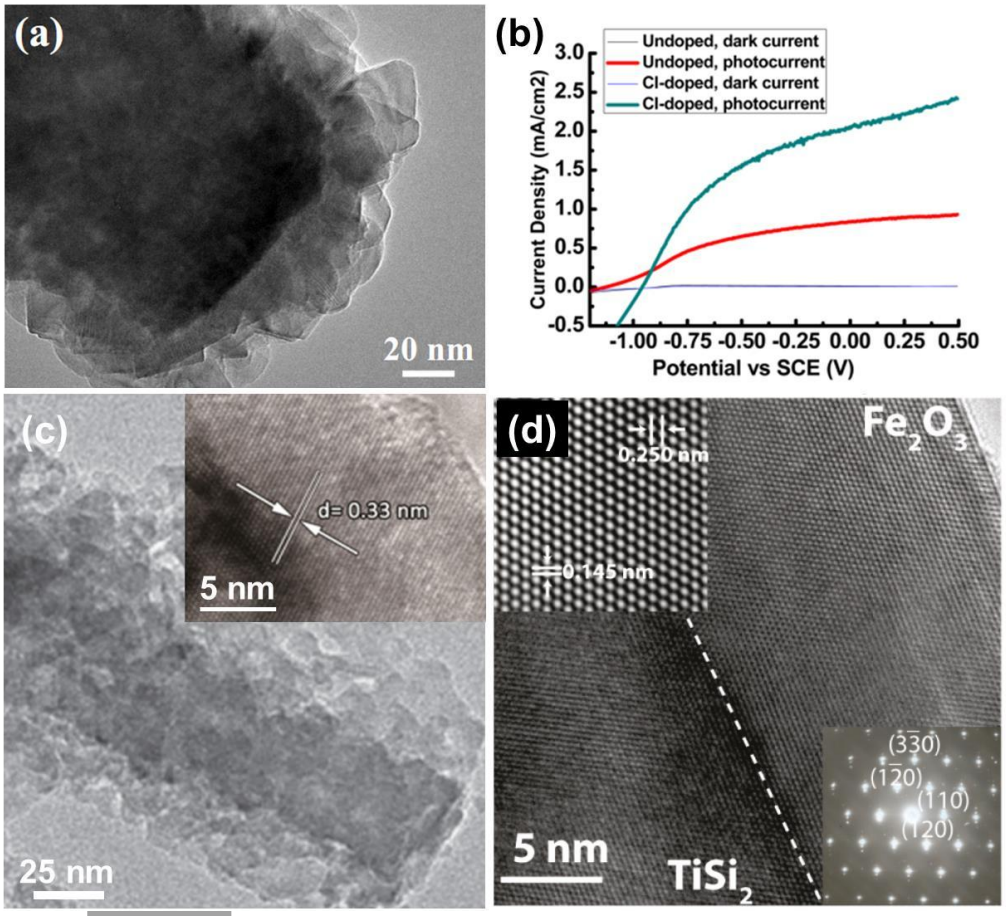

Figure 2. a) TEM image of a Cl-doped ZnO NW fully coated with polycrystalline anatase TiO_2. b) J–V characteristics of two photoanodes based on undoped and Cl-doped ZnO NW arrays. Reproduced with permission.[8d] Copyright 2014, American Chemical Society. c) TEM image of Si/Bi_2O_3 core–shell NW structures. Inset is the HRTEM images of core–shell NWs with 30 nm Bi_2O_3. Reproduced with permission.[15] Copyright 2014, IOP Publishing Ltd. d) HRTEM of $TiSi_2$ core/hematite shell structure. Insets: (left) lattice-fringe-resolved HRTEM image showing the hematite lattice spacing for (110) (0.250 nm) and (330) (0.145 nm); (right) electron diffraction pattern of hematite. Reproduced with permission.[16a] Copyright 2011, American Chemical Society.

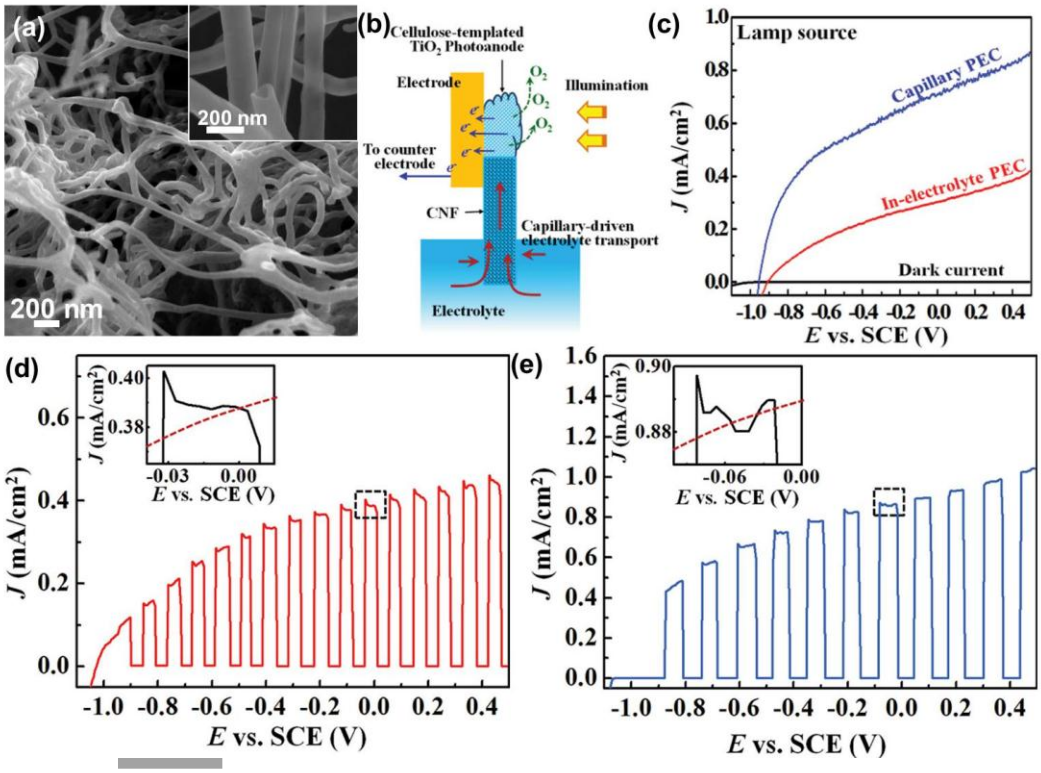

Figure 3. a) Fibrous TiO_2 nanotube network after annealing at 600 ºC for 24 hours; inset shows a broken tip revealing the hollow tubular structure. b) Schematic illustration of the capillary PEC setup. c) J–V characteristics of a cellulose-templated TiO_2 photoanode measured using capillary setup and in-electrolyte setup under 100 mW cm^{-2} Xe lamp source. d, e) J–V characteristics of cellulose-templated TiO_2 photoanodes measured under interrupted illumination using in-electrolyte PEC setup (d) and capillary PEC setup (e). Insets are enlarged top regions of one J_{ph} cycle showing the feature of the initial current spikes. Reproduced with permission.[17] Copyright 2014, Wiley.

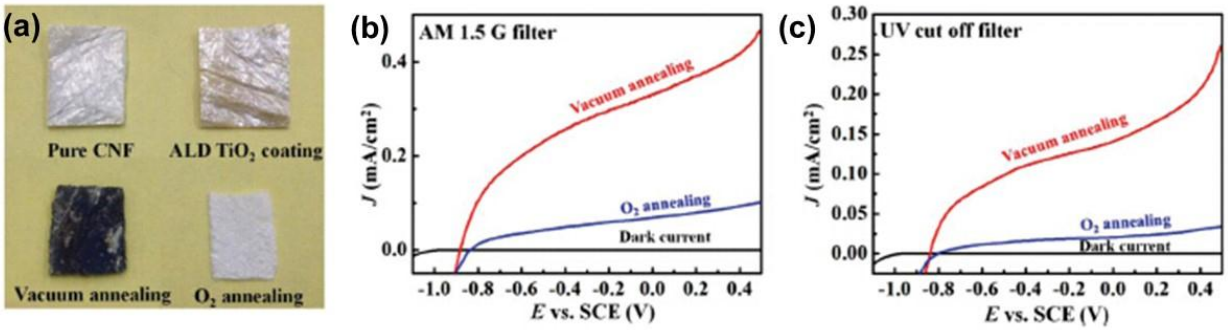

Figure 4. a) Photos of CNF films before and after TiO_2 coating, and after annealing in vacuum and oxygen atmosphere. b, c) Performance comparisons of cellulose-templated TiO_2 photoanodes annealed in vacuum (red curves) and in oxygen (blue curves) measured with AM 1.5G filter (b) and UV cutoff filter (c). Reproduced with permission.[17] Copyright 2014, Wiley.

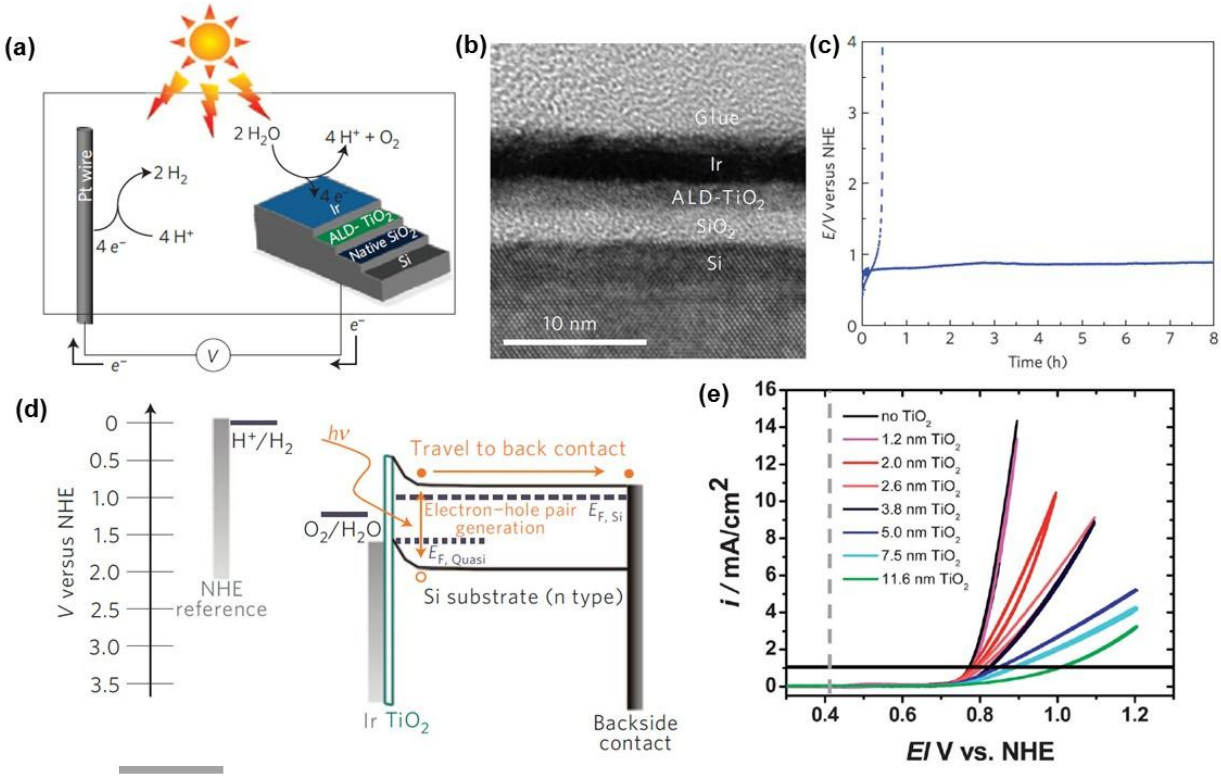

Figure 5. a) Schematic and (b) cross-sectional TEM image of the Si/TiO_2/Ir photoanode. c) Voltage-time curve of the photoanode with (solid line) and without (dashed line) TiO_2 protection layer at a constant photocurrent density of 5 mA cm^{-2} upon 1 sun solar illumination in 1 M alkaline electrolyte. d) Approximate energy band diagram of Si/TiO_2/Ir photoanode at 1V versus NHE under illumination in pH=0 solution. Reproduced with permission.[24] Copyright 2011, Nature Publishing Group. e) Current density versus potential curves of Ir/x nm of TiO_2/SiO_2/p^+-Si electrodes in the alkaline solution. Reproduced with permission.[25a] Copyright 2013, Royal Society of Chemistry.

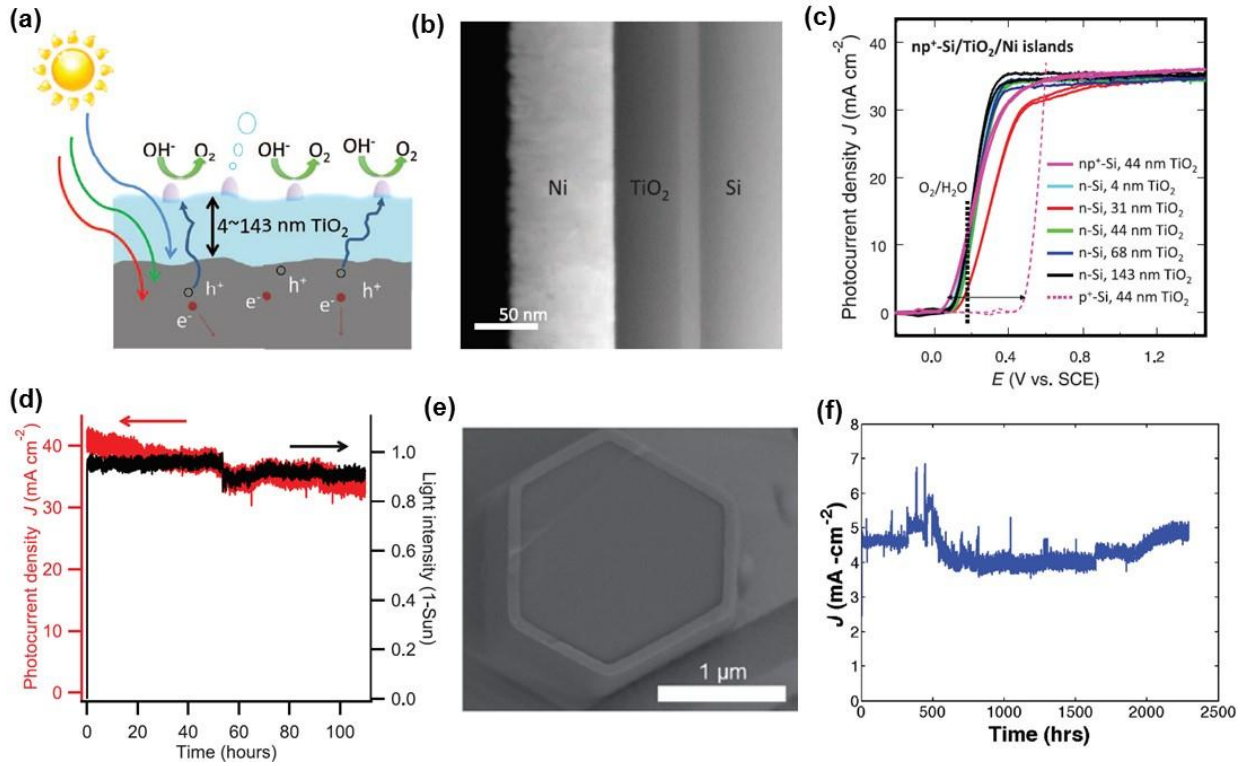

Figure 6. a) Cross-sectional schematic and (b) TEM image of the silicon photoanode stabilized by a thick and electronically defective ALD amorphous TiO_2. c) Photocurrent density versus potential (*J-V*) plot of the Si photoanodes coated by protective TiO_2 with various thicknesses in 1M KOH under 1.25 Sun illumination. d) Photocurrent density versus time (*J-t*) curve of a np^+-Si photoanode coated with 44 nm TiO_2 and Ni islands in 1 M KOH at a constant bias of 0.93 V versus SCE. Reproduced with permission.[26] Copyright 2014, The American Association for the Advancement of Science. e) Cross-sectional SEM image of an individual ALD TiO_2 coated silicon microwire. f) *J-t* plot for a np^+-Si /TiO_2/$NiCrO_x$ microwire photoanode in 1 M KOH under 1 sun illumination at a constant bias of 0.36 V vs $E^{O'}(OH^-/O_2)$. Reproduced with permission.[29] Copyright 2014, Royal Society of Chemistry.

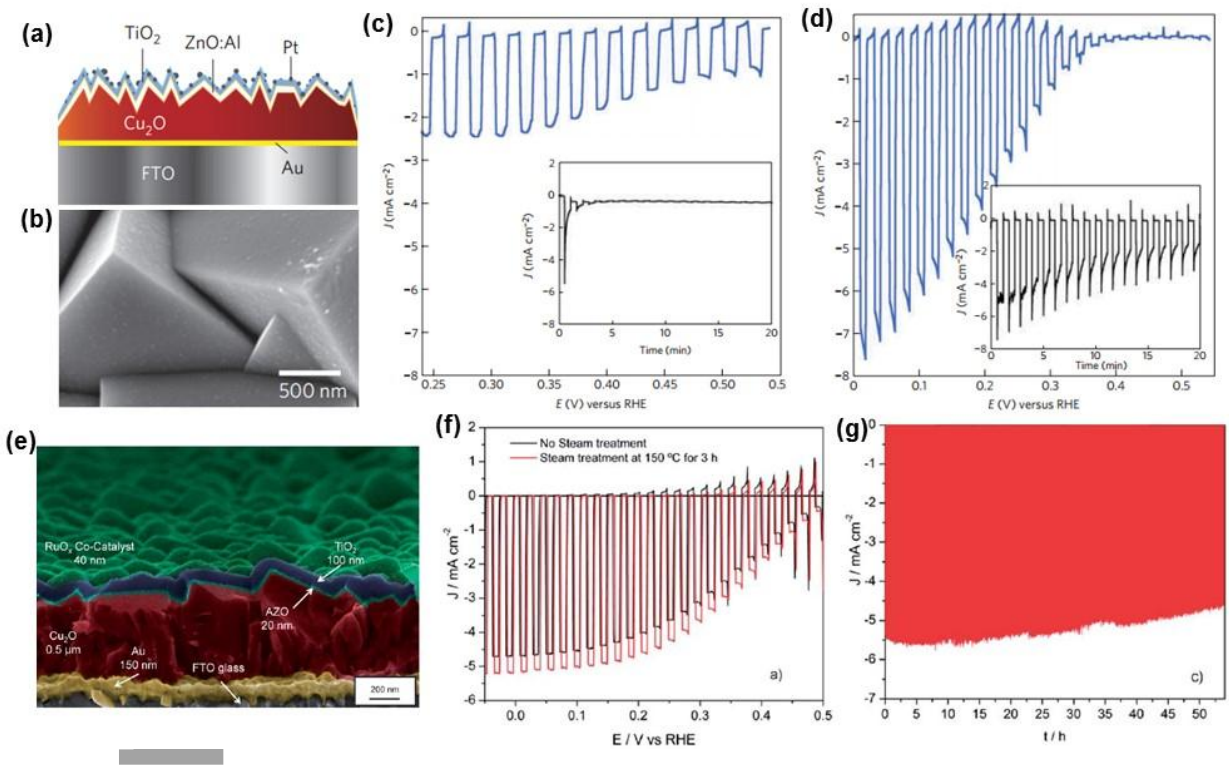

Figure 7. a) Cross-sectional schematic and (b) top-view SEM image of the surface-protected Cu_2O photocathode. c,d) *J-V* plot of the bare Cu_2O **(c)** and Cu_2O with 20 nm AZO and 11 nm TiO_2 (d) photocathodes in 1 M Na_2SO_4 solution under chopped AM 1.5 light illumination. Insets are corresponding *J-t* curves. Reproduced with permission.[32] Copyright 2011, Nature Publishing Group. e) Cross-sectional SEM image of ALD-protected Cu_2O photocathode after the steam treatment. f) *J-V* plots of the ALD-protected Cu_2O photocathode before (black) and after (red) steam treatment at 150 °C for 3 hours in pH=5.0 phosphate-sulfate electrolyte under chopped light illumination. g) *J-t* characterization of the ALD-protected and steam-treated Cu_2O photocathode measured in pH=5.0 phosphate-sulfate electrolyte under chopped light illumination at bias of 0 V vs vs RHE. Reproduced with permission.[33] Copyright 2014, Royal Society of Chemistry.

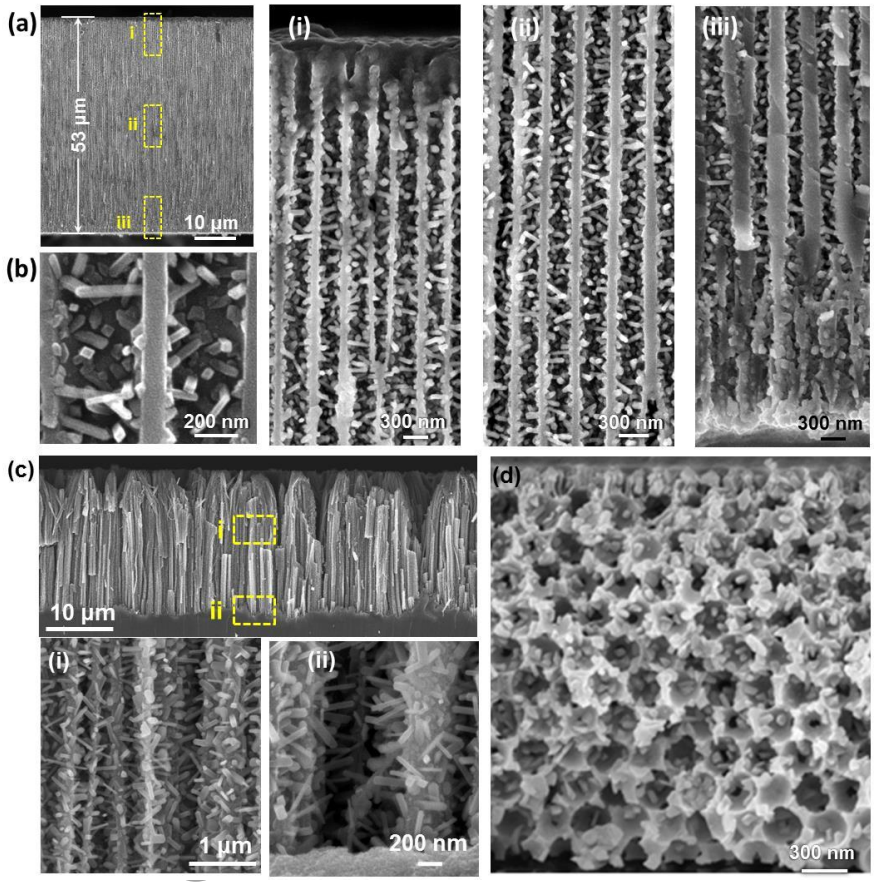

Figure 8. a) The uniform and dense coating of SPCVD TiO_2 NRs inside the AAO channels at the top (i), middle (ii), and bottom (iii) sections. b) Higher magnification SEM of TiO_2 NRs rooted on the walls of AAO channels. Reproduced with permission.[34] Copyright 2011, American Chemical Society. c) SPCVD TiO_2 NRs on 25µm long Si NWs. Reproduced with permission.[8c] Copyright 2011, American Chemical Society. d) SPCVD of TiO_2 NRs inside inverse opal.

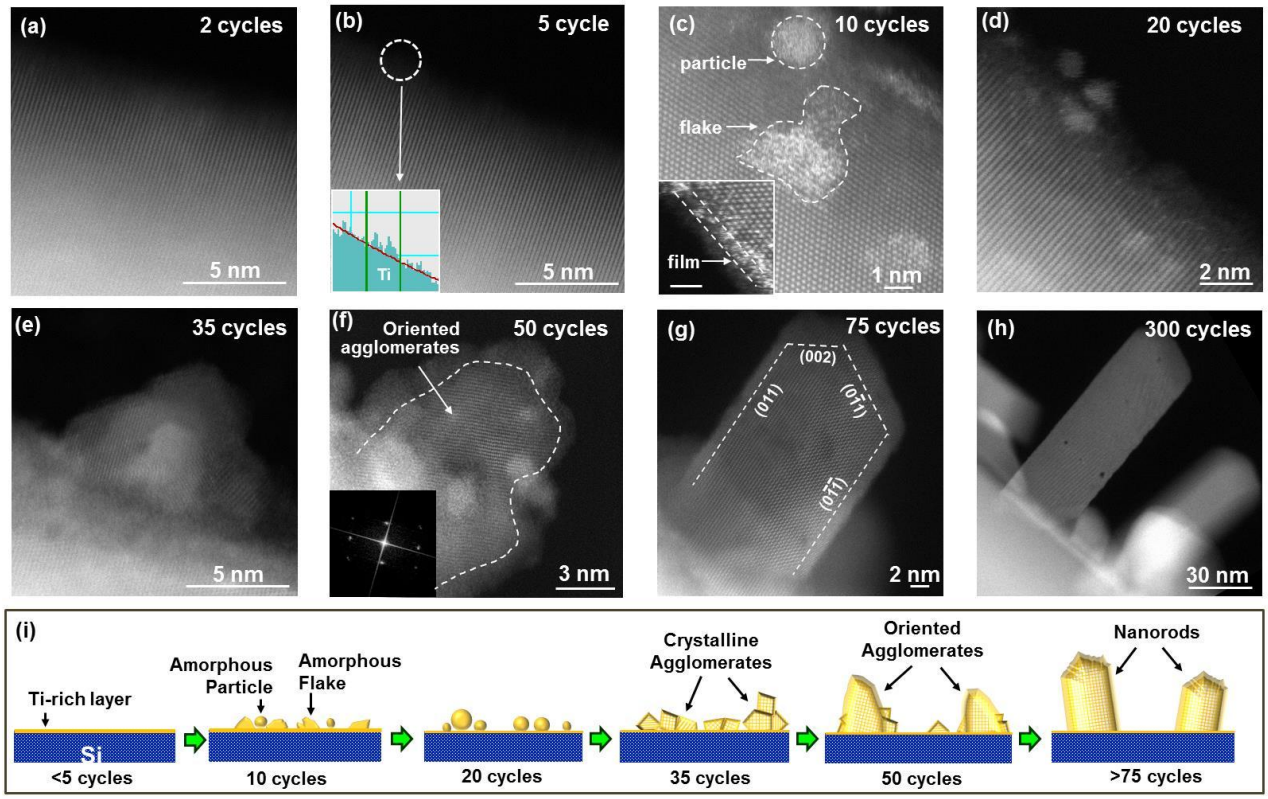

Figure 9. Evolution of TiO_2 NRs at different ALD cycles at 600 °C. a–h) STEM image of TiO2 on Si surface after 2, 5, 10, 20, 35, 50, 75 and 300 cycle growth, respectively. Inset of (b): EELS analysis on 5 cycle sample detected the existence of Ti. Inset of (c) shows the amorphous ultrathin TiO_x layer coated on NW substrate (scale bar is 1 nm). Inset of (f) is the FFT pattern converted from lattice image. i) Schematic illustration the entire evolution process of TiO_2 NRs. Scale bars are 5 nm unless otherwise noted. Reproduced with permission.[35] Copyright 2013, American Chemical Society.

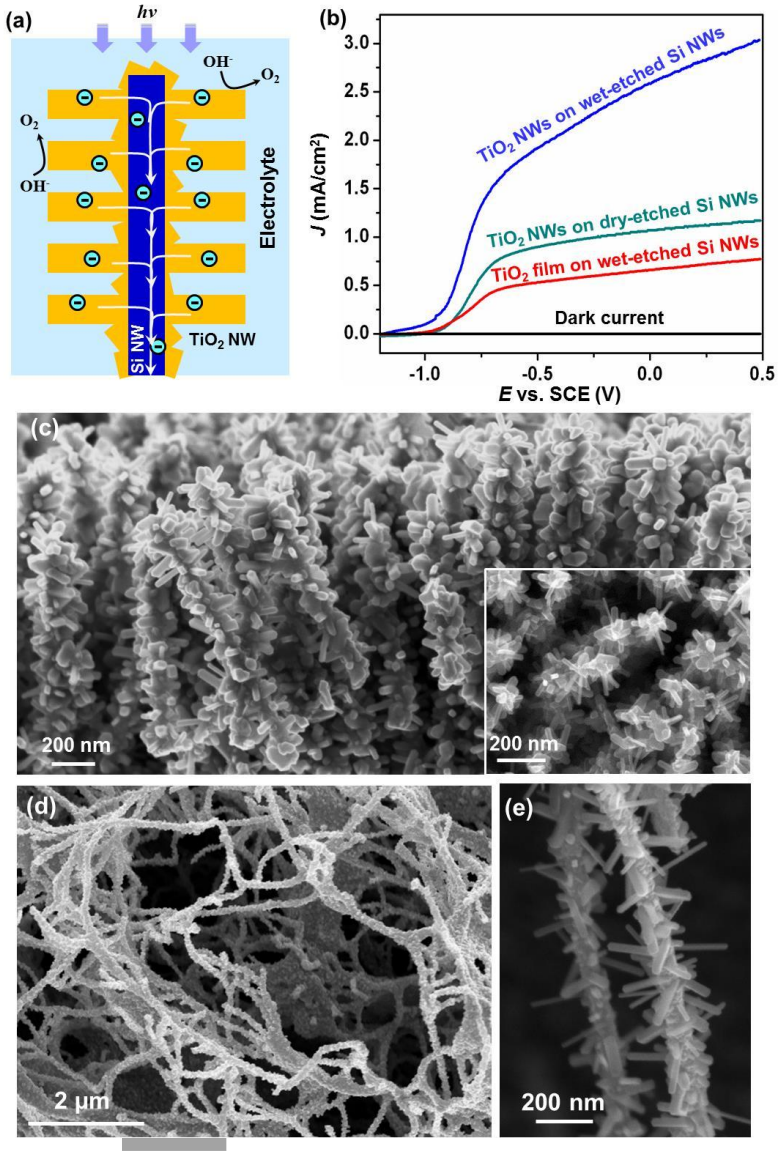

Figure 10. a) Schematic illustration of using TiO_2-Si NW structure as PEC anode for water splitting. b) J-E curves of different TiO_2-Si configurations showing enhanced PEC performance by introducing high-density TiO_2 NR branches. Reproduced with permission.[8c] Copyright 2011, American Chemical Society. c) Cross-sectional SEM image of a 3D TiO_2 nanoforest formed on ZnO NWs. Inset is the top view. Reproduced with permission.[36] Copyright 2014, American Chemical Society. d) Fibrous network morphology observed after SPCVD TiO_2 NR growth. e) TiO_2 NR coverage and morphology on individual CNFs. Reproduced with permission.[37] Copyright 2014, IOP Publishing Ltd.

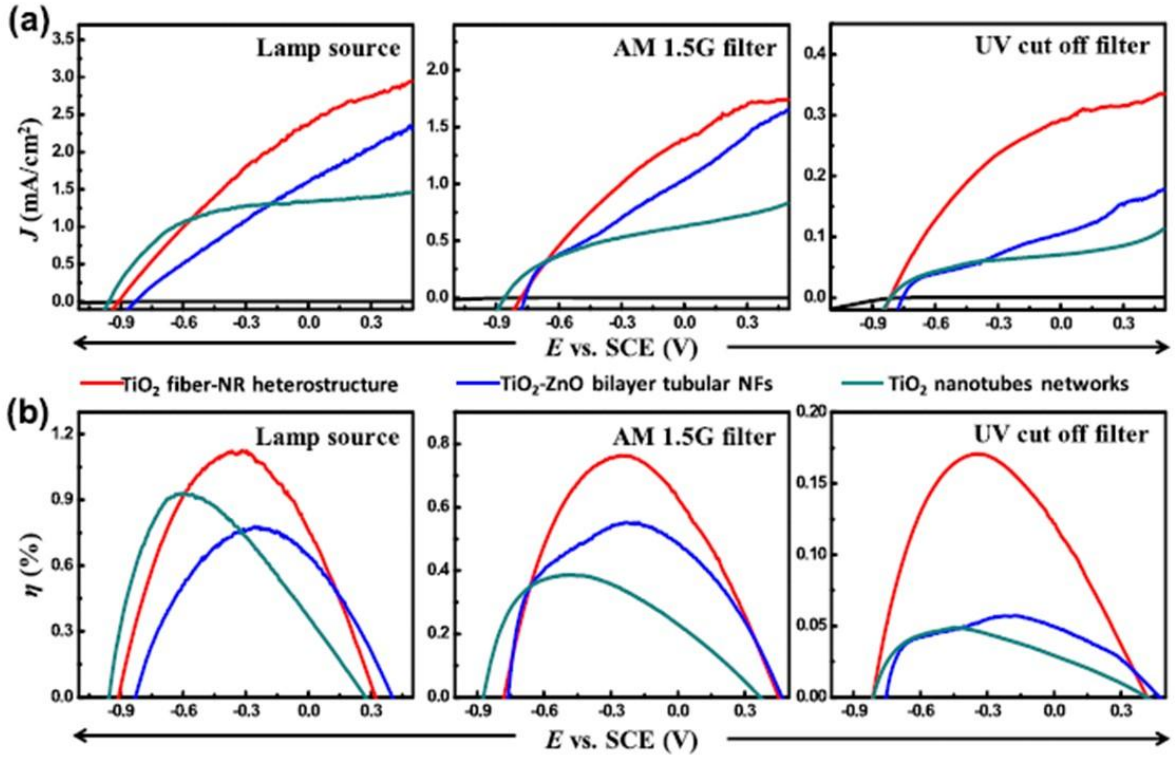

Figure 11. a) Photoelectrochemical performance of three CNF-templated fibrous networks under illuminations of a 100 mW cm^{-2} Xe lamp source, a lamp with an AM 1.5G filter, and with a UV cutoff filter. b) Corresponded PEC efficiencies for these CNF-templated 3D architectures. Reproduced with permission.[37] Copyright 2014, IOP Publishing Ltd.

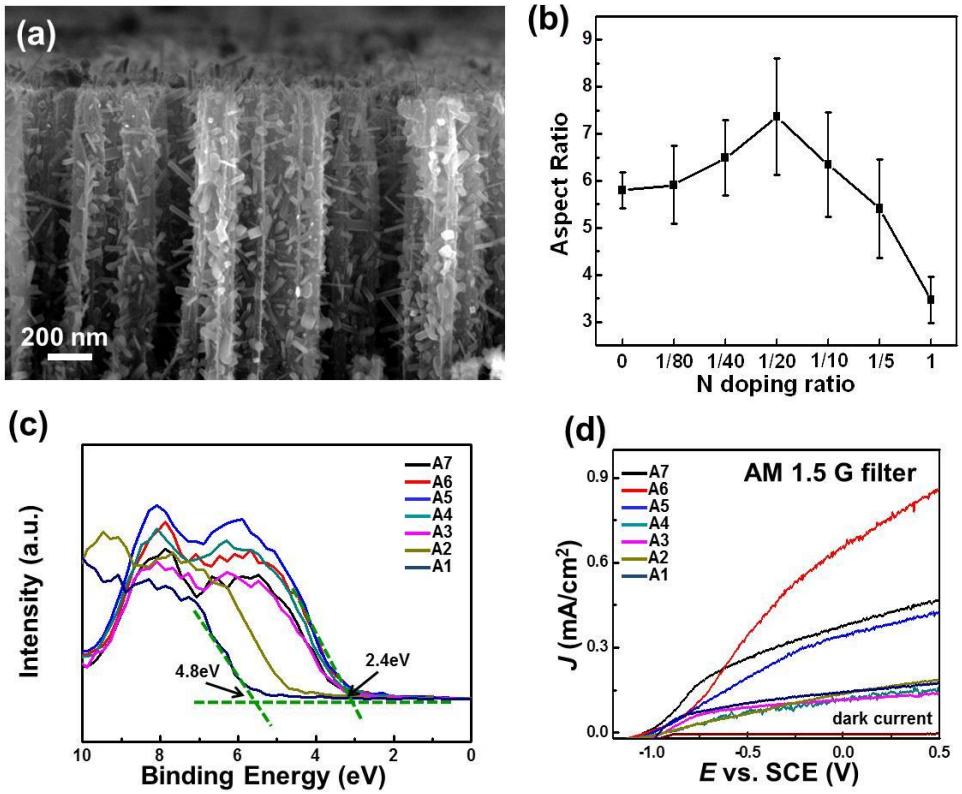

Figure 12. a) Cross-section view of high-density Nitrogen doped TiO_2 NRs on Si NW arrays. b) Plots of aspect ratio of NRs as a function of Nitrogen doping ratio. c) XPS demonstrates that density of states (DOS) shift in the valence band. d) J-V curves of Nitrogen doped and undoped TiO_2 NRs-Si NW hierarchical architectures under illuminations of 100 mW cm^{-2} Xe lamp source with AM 1.5G filter. Reproduced with permission.[20b] Copyright 2015, American Chemical Society.

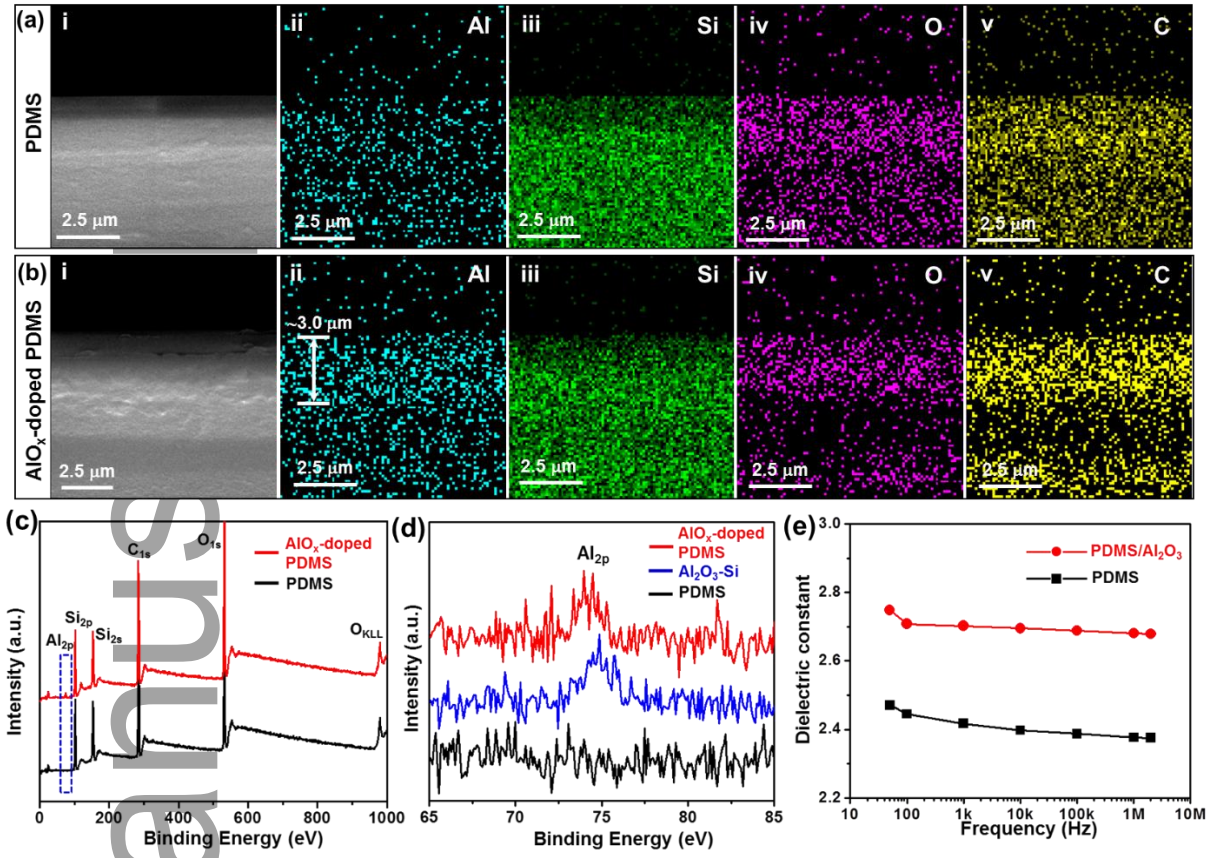

Figure 13. a, b) Cross-sectional SEM images (i) and EDS mappings of a pristine PDMS film (a) and an AlO_x-doped PDMS film (b) for Al, Si, O, and C elements (ii-v). c) Full range XPS spectra acquired from pristine PDMS and AlO_x-doped PDMS. Small Al 2p peak was identified on the spectrum of AlO_x-doped PDMS. d) Al 2p scan for pristine PDMS, AlO_x-doped PDMS film and ALD grown Al_2O_3 on silicon substrate. The peak position shift indicates the presence of defective oxides in AlO_x-doped PDMS film. e) Dielectric constant measured from pristine PDMS and AlO_x-doped PDMS, showing increased dielectric constant of PDMS due to the AlO_x doping. Reproduced with permission.[6a] Copyright 2015, Wiley.

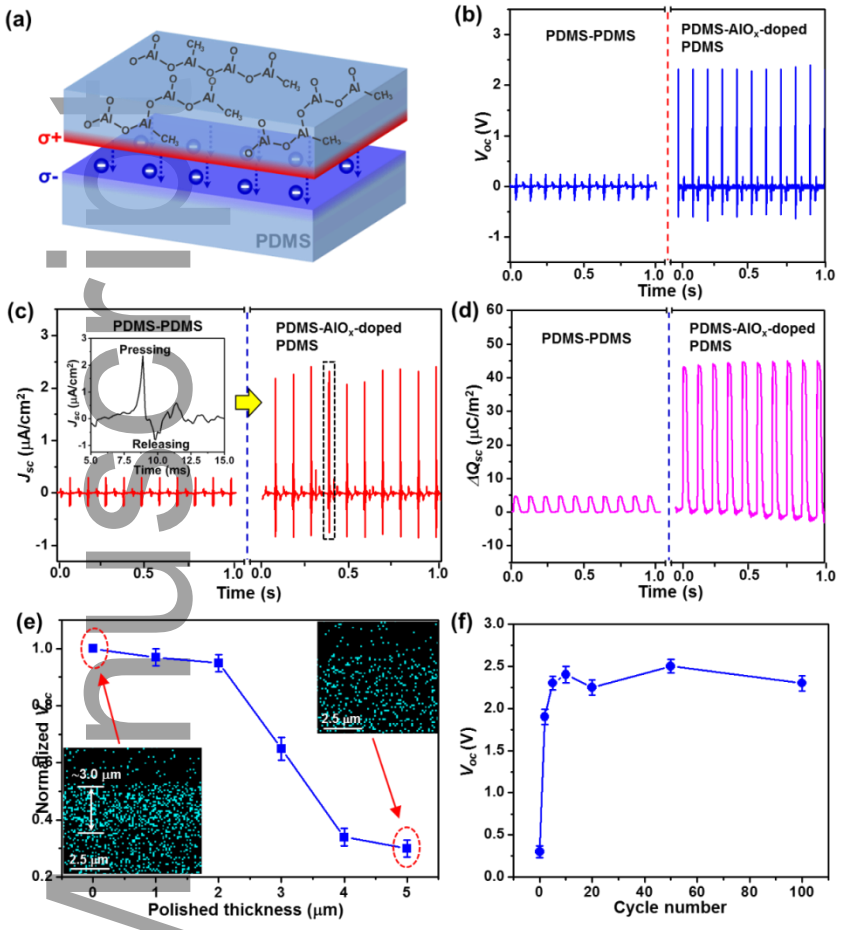

Figure 14. a) Schematic of charge redistribution between pristine PDMS and AlO_x-doped PDMS films upon contact as a consequence of triboelectrification. b) The V_{oc}, (c) J_{sc} and (d) charge transfer amount under short-circuit condition (ΔQ_{sc}) of TENGs built from PDMS with and without AlO_x doping. The inset of (c) is the enlarged current output (generated by one pressing and releasing cycle. e) Normalized V_{oc} of TENGs as a function of the material thickness that was polished off. Voltage output of AlO_x-doped PDMS film without any polishing was defined as unit. Insets are Al element EDS mapping of AlO_x-doped PDMS films before (left) and after (right) ≈5 μm polishing. f) V_{oc} variation versusversus the doping cycles of AlO_x on PDMS film. Reproduced with permission.[6a] Copyright 2015, Wiley.

References <comp>TYPESETTER: Please abbreviate all journal names in references section as per journal style.</comp>

[1] S. M. George, *Chem. Rev.* **2010**, *110*, 111.

[2] M. Ritala, M. Leskela, *Handbook of Thin Film Materials* **2001**, *1*, 103.

[3] D. S. Guan, J. A. Jeevarajan, Y. Wang, *Nanoscale* **2011**, *3*, 1465.

[4] R. L. Puurunen, *J. Appl. Phys.* **2005**, *97*.

[5] Z. P. Rao, J. Wan, C. B. Li, B. Chen, J. Liu, C. Q. Huang, Y. Xia, *Plasma Science & Technology* **2014**, *16*, 239.

[6] a) Y. Yu, Z. Li, Y. Wang, S. Gong, X. Wang, *Adv. Mater.* **2015**, *27*, 4938; b) S. Hu, N. S. Lewis, J. W. Ager, J. Yang, J. R. McKone, N. C. Strandwitz, *The Journal of Physical Chemistry C* **2015**, *119*, 24201; c) N. S. Lewis, *Science* **2016**, *351*, aad1920; d) M. F. Lichterman, K. Sun, S. Hu, X. Zhou, M. T. McDowell, M. R. Shaner, M. H. Richter, E. J. Crumlin, A. I. Carim, F. H. Saadi, B. S. Brunschwig, N. S. Lewis, *Catal. Today* **2016**, *262*, 11.

[7] a) R. W. Johnson, A. Hultqvist, S. F. Bent, *Mater. Today* **2014**, *17*, 236; b) O. Nilsen, V. Miikkulainen, K. B. Gandrud, E. Ostreng, A. Ruud, H. Fjellvag, *Physica Status Solidi a-Applications and Materials Science* **2014**, *211*, 357; c) X. R. Wang, G. Yushin, *Energy & Environmental Science* **2015**, *8*, 1889; d) B. Ahmed, C. Xia, H. N. Alshareef, *Nano Today* **2016**, *11*, 250; e) S. Fleischmann, N. Jackel, M. Zeiger, B. Kruner, I. Grobelsek, P. Formanek, S. Choudhury, D. Weingarth, V. Presser, *Chem. Mater.* **2016**, *28*, 2802.

[8] a) W.-J. Yin, H. Tang, S.-H. Wei, M. M. Al-Jassim, J. Turner, Y. Yan, *Physical Review B* **2010**, *82*; b) S. W. Boettcher, J. M. Spurgeon, M. C. Putnam, E. L. Warren, D. B. Turner-Evans, M. D. Kelzenberg, J. R. Maiolo, H. A. Atwater, N. S. Lewis, *Science* **2010**, *327*, 185; c) J. Shi, Y. Hara, C. Sun, M. A. Anderson, X. Wang, *Nano Lett.* **2011**, *11*, 3413; d) F. Wang, J. H. Seo, Z. Li, A. V. Kvit, Z. Ma, X. Wang, *ACS Appl Mater Interfaces* **2014**, *6*, 1288.

[9] B. J. O'Neill, D. H. K. Jackson, J. Lee, C. Canlas, P. C. Stair, C. L. Marshall, J. W. Elam, T. F. Kuech, J. A. Dumesic, G. W. Huber, *Acs Catalysis* **2015**, *5*, 1804.

[10] a) Z. L. Wang, *Acs Nano* **2013**, *7*, 9533; b) F. R. Fan, Z. Q. Tian, Z. L. Wang, *Nano Energy* **2012**, *1*, 328.

[11] T. Wang, Z. Luo, C. Li, J. Gong, *Chem. Soc. Rev.* **2014**, *43*, 7469.

[12] a) X. Wang, Z. Li, J. Shi, Y. Yu, *Chem. Rev.* **2014**, *114*, 9346; b) A. J. Nozik, *Ann. Rev. Phys. Cher.* **1978**, *29*, 34.

[13] Q. Peng, B. Kalanyan, P. G. Hoertz, A. Miller, H. Kim do, K. Hanson, L. Alibabaei, J. Liu, T. J. Meyer, G. N. Parsons, J. T. Glass, *Nano Lett.* **2013**, *13*, 1481.

[14] J. H. Noh, B. Ding, H. Soo Han, J. Seong Kim, *Appl. Phys. Lett.* **2012**, *100*, 084104.

[15] B. Weng, F. Xu, J. Xu, *Nanotechnology* **2014**, *25*, 455402.

[16] a) L. Yongjing, Z. Sa, S. W. Sheehan, W. Dunwei, *J. Am. Chem. Soc.* **2011**, *133*, 2398; b) L. Yongjing, Z. Sa, L. Xiaohua, S. Stafford, W. Dunwei, *J. Am. Chem. Soc.* **2009**, *131*, 2772.

[17] Z. Li, C. Yao, Y. Yu, Z. Cai, X. Wang, *Adv. Mater.* **2014**, *26*, 2262.

[18] a) F. Le Formal, N. Tétreault, M. Cornuz, T. Moehl, M. Grätzel, K. Sivula, *Chem. Sci.* **2011**, *2*, 737; b) G. Horowitz, *Journal of Electroanalytical Chemistry and Interfacial Electrochemistry* **1983**, *159*, 421; c) C. Sanchez, K. D. Sieber, G. A. Somorjai, *Journal of Electroanalytical Chemistry and Interfacial Electrochemistry* **1988**, *252*, 269; d) M. P. Dare-Edwards, J. B. Goodenough, A. Hamnett, P. R. Trevellick, *Journal of the Chemical Society, Faraday Transactions 1: Physical Chemistry in Condensed Phases* **1983**, *79*, 2027.

[19] X. Ming, D. Peimei, W. Haoyu, Z. Dongyuan, Z. Gengfeng, *Nano Lett.* **2012**, *12*, 1503.

[20] a) V. Pore, M. Heikkilä, M. Ritala, M. Leskelä, S. Areva, *J. Photochem. Photobiol. A: Chem.* **2006**, *177*, 68; b) Z. Li, F. Wang, A. Kvit, X. Wang, *The Journal of Physical Chemistry C* **2015**, *119*, 4397; c) H.-E. Cheng, Y.-R. Chen, W.-T. Wu, C.-M. Hsu, *Materials Science and Engineering: B* **2011**, *176*, 596.

[21] Y. Lin, X. Yang, M. T. Mayer, Z. I. Simpson, G. Mcmahon, S. Zhou, D. Wang, *J. Am. Chem. Soc.* **2012**, *134*, 5508.

[22] M. G. Walter, E. L. Warren, J. R. McKone, S. W. Boettcher, Q. Mi, E. A. Santori, N. S. Lewis, *Chem. Rev.* **2010**, *110*, 6446.

[23] a) M. J. Kenney, M. Gong, Y. Li, J. Z. Wu, J. Feng, M. Lanza, H. Dai, *Science* **2013**, *342*, 836; b) L. Ji, M. D. McDaniel, S. Wang, A. B. Posadas, X. Li, H. Huang, J. C. Lee, A. A. Demkov, A. J. Bard, J. G. Ekerdt, E. T. Yu, *Nat Nanotechnol* **2015**, *10*, 84; c) K. Sun, F. H. Saadi, M. F. Lichterman, W. G. Hale, H. P. Wang, X. Zhou, N. T. Plymale, S. T. Omelchenko, J. H. He, K. M. Papadantonakis, B. S. Brunschwig, N. S. Lewis, *Proc. Natl. Acad. Sci. U. S. A.* **2015**, *112*, 3612.

[24] Y. W. Chen, J. D. Prange, S. Duhnen, Y. Park, M. Gunji, C. E. Chidsey, P. C. McIntyre, *Nat Mater* **2011**, *10*, 539.

[25] a) A. G. Scheuermann, J. D. Prange, M. Gunji, C. E. D. Chidsey, P. C. McIntyre, *Energy & Environmental Science* **2013**, *6*, 2487; b) A. G. Scheuermann, J. P. Lawrence, K. W. Kemp, T. Ito, A. Walsh, C. E. Chidsey, P. K. Hurley, P. C. McIntyre, *Nat Mater* **2016**, *15*, 99.

[26] S. Hu, M. R. Shaner, J. A. Beardslee, M. Lichterman, B. S. Brunschwig, N. S. Lewis, *Science* **2014**, *344*, 1005.

[27] J. Qiu, G. Zeng, M.-A. Ha, B. Hou, M. Mecklenburg, H. Shi, A. N. Alexandrova, S. B. Cronin, *Chem. Mater.* **2015**, *27*, 7977.

[28] J. Gu, Y. Yan, J. L. Young, K. X. Steirer, N. R. Neale, J. A. Turner, *Nat Mater* **2015**.

[29] M. R. Shaner, S. Hu, K. Sun, N. S. Lewis, *Energy Environ. Sci.* **2015**, *8*, 203.

[30] M. F. Lichterman, A. I. Carim, M. T. McDowell, S. Hu, H. B. Gray, B. S. Brunschwig, N. S. Lewis, *Energy Environ. Sci.* **2014**, *7*, 3334.

[31] M. T. McDowell, M. F. Lichterman, J. M. Spurgeon, S. Hu, I. D. Sharp, B. S. Brunschwig, N. S. Lewis, *The Journal of Physical Chemistry C* **2014**, *118*, 19618.

[32] A. Paracchino, V. Laporte, K. Sivula, M. Grätzel, E. Thimsen, *Nature materials* **2011**, *10*, 456.

[33] J. Azevedo, L. Steier, P. Dias, M. Stefik, C. T. Sousa, J. P. Araújo, A. Mendes, M. Graetzel, S. D. Tilley, *Energy Environ. Sci.* **2014**, *7*, 4044.

[34] J. Shi, C. Sun, M. B. Starr, X. Wang, *Nano letters* **2011**, *11*, 624.

[35] J. Shi, Z. D. Li, A. Kvit, S. Krylyuk, A. V. Davydov, X. D. Wang, *Nano Lett.* **2013**, *13*, 5727.

[36] Y. Yu, X. Yin, A. Kvit, X. Wang, *Nano Lett.* **2014**, *14*, 2528.

[37] Z. Li, C. Yao, F. Wang, Z. Cai, X. Wang, *Nanotechnology* **2014**, *25*, 504005.

[38] a) M. Biswas, J. A. Libera, S. B. Darling, J. W. Elam, *The Journal of Physical Chemistry C* **2015**, *119*, 14585; b) Q. Peng, Y. C. Tseng, S. B. Darling, J. W. Elam, *ACS Nano* **2011**, *5*, 4600; c) C. A. Wilson, R. K. Grubbs, S. M. George, *Chem. Mater.* **2005**, *17*, 5625.

[39] a) Q. Peng, Y. C. Tseng, S. B. Darling, J. W. Elam, *Adv. Mater.* **2010**, *22*, 5129; b) R. Saberi Moghaddam, S. Huettner, Y. Vaynzof, C. Ducati, G. Divitini, R. H. Lohwasser, K. P. Musselman, A. Sepe, M. R. Scherer, M. Thelakkat, U. Steiner, R. H. Friend, *Nano Lett.* **2013**, *13*, 4499; c) Y.-C. Tseng, Q. Peng, L. E. Ocola, J. W. Elam, S. B. Darling, *The Journal of Physical Chemistry C* **2011**, *115*, 17725.

[40] Y. Yu, X. Wang, *Extreme Mechanics Letters* **2016**.

[41] a) G. Zhu, Y. S. Zhou, P. Bai, X. S. Meng, Q. Jing, J. Chen, Z. L. Wang, *Advanced materials* **2014**, *26*, 3788; b) Y. Xie, S. Wang, S. Niu, L. Lin, Q. Jing, J. Yang, Z. Wu, Z. L. Wang, *Advanced materials* **2014**, *26*, 6599.

[42] E. Dickey, W. A. Barrow, *Journal of Vacuum Science & Technology A* **2012**, *30*, 021502.

[43] a) J. R. Wank, S. M. George, A. W. Weimer, *Powder Technol.* **2004**, *142*, 59; b) J. R. Wank, S. M. George, A. W. Weimer, *J. Am. Ceram. Soc.* **2004**, *87*, 762; c) J. Ferguson, K. Buechler, A. Weimer, S. George, *Powder Technol.* **2005**, *156*, 154; d) D. Longrie, D. Deduytsche, J. Haemers, K. Driesen, C. Detavernier, *Surf. Coat. Technol.* **2012**, *213*, 183.

[44] a) P. Poodt, A. Lankhorst, F. Roozeboom, K. Spee, D. Maas, A. Vermeer, *Adv. Mater.* **2010**, *22*, 3564; b) D. Muñoz-Rojas, M. Jordan, C. Yeoh, A. Marin, A. Kursumovic, L. Dunlop, D. Iza, A. Chen, H. Wang, J. M. Driscoll, *AIP Advances* **2012**, *2*, 042179.

Atomic Layer Deposition for Advanced Electrode Design in Photoelectrochemical and Triboelectric Systems

J. Su, Z. Li, Y.Yu, X.Wang*

On the basis of sequential self-limiting surface reactions, atomic layer deposition is capable of growing high quality, pinhole-free and conformal thin films as well as 3D nanoarchitectures, promoting advanced design and manufacture of highly-efficient and extremely-stable photoelectrochemical electrodes and triboelectric nanogenerators.

Biographies

<qry>Please include up to 3 author biographies (max. 100 words) here. Please also send us author photographs for the biographies by email.</qry>